

Concentration Polarization of Interacting Solute Particles in Cross-Flow Membrane Filtration

Subir Bhattacharjee, Albert S. Kim,¹ and Menachem Elimelech²

Department of Chemical Engineering, Yale University, 9 Hillhouse Avenue, New Haven, Connecticut 06520-8286

Received July 29, 1998, accepted December 17, 1998

A theoretical approach for predicting the influence of interparticle interactions on concentration polarization and the ensuing permeate flux decline during cross-flow membrane filtration of charged solute particles is presented. The Ornstein–Zernike integral equation is solved using appropriate closures corresponding to hard-spherical and long-range solute–solute interactions to predict the radial distribution function of the solute particles in a concentrated solution (dispersion). Two properties of the solution, namely the osmotic pressure and the diffusion coefficient, are determined on the basis of the radial distribution function at different solute concentrations. Incorporation of the concentration dependence of these two properties in the concentration polarization model comprising the convective-diffusion equation and the osmotic-pressure governed permeate flux equation leads to the coupled prediction of the solute concentration profile and the local permeate flux. The approach leads to a direct quantitative incorporation of solute–solute interactions in the framework of a standard theory of concentration polarization. The developed model is used to study the effects of ionic strength and electrostatic potential on the variations of solute diffusivity and osmotic pressure. Finally, the combined influence of these two properties on the permeate flux decline behavior during cross-flow membrane filtration of charged solute particles is predicted. © 1999 Academic Press

Key Words: concentration polarization; cross-flow membrane filtration; permeate flux decline; Ornstein–Zernike equation; osmotic pressure; sedimentation; diffusion.

1. INTRODUCTION

Concentration polarization during cross-flow membrane filtration and the ensuing permeate flux decline are generally modeled by coupling the convective-diffusion equation with an appropriate expression governing the permeate transport. This coupled model for concentration polarization and flux decline may be regarded as the cornerstone of our theoretical understanding of membrane filtration involving a diverse array of colloidal and macromolecular systems (1–5).

The above macroscopic continuum model, even in its most

general formulation, often fails to provide a complete theoretical perspective of the flux decline behavior. This limitation is apparent from the inability of the model to accurately and independently predict the permeate flux behavior for a wide range of solutes. The shortcomings of the theory have often been ascribed to the use of inappropriate expressions for transmembrane permeate transport. Rather indiscriminate use of the thermodynamic (osmotic pressure model) and hydrodynamic (filtration theory) approaches to model the transmembrane transport led to considerable confusion regarding the actual mechanism of concentration polarization and flux decline during the past two decades (1–4). However, it gradually became transparent that these two approaches might be equivalent, particularly when modeling the concentration polarization phenomenon of solute particles in the absence of a cake layer buildup (6). Recently, it was shown that the osmotic pressure and filtration (hydrodynamic) approaches constitute equivalent alternative descriptions of the concentration polarization phenomenon (5, 7). Despite these advancements, however, a priori predictions of permeate flux based on solution and membrane properties still remain elusive.

The inability of the convective-diffusion model to predict the permeate flux accurately may also be ascribed to the absence of any information regarding the physicochemical interactions between the solute particles in the model framework. Two parameters in the convective-diffusion model, namely the osmotic pressure and the gradient (mutual) diffusion coefficient, are generally supplied in the form of experimental correlations or are used as adjustable parameters (2, 6, 8, 9). Embedded in these two macroscopic properties is an astounding amount of information regarding the physicochemical interactions between the solute particles in the polarized layer and the solution structure engendered by such interactions. Use of experimental correlations for concentration dependence of osmotic pressure or empirical values of diffusion coefficient does not provide a quantitative understanding of these interparticle interactions. The paucity of a sound theoretical link between these macroscopic properties and the interparticle interactions often renders the convective-diffusion model of flux decline semiempirical, capable only of fitting experimental data using adjustable parameters.

¹ Present address: School of Engineering and Applied Science, University of California, Los Angeles, CA 90095-1593.

² To whom correspondence should be addressed. E-mail: menachem.elimelech@yale.edu.



A comprehensive predictive theory of flux decline should relate the physicochemical interactions between the solute particles in the polarized layer to the osmotic pressure and the diffusion coefficient. The resulting estimates of diffusion coefficient and osmotic pressure, when substituted in the flux decline model, may render the macroscopic model capable of quantifying the influence of interparticle interactions on permeate flux decline. Incorporation of interparticle interactions in models of flux decline has received considerable attention over the recent years (10–18). The first quantitative incorporation of interparticle interactions to investigate permeate flux decline behavior was motivated by experimental observations of the effect of particle charge, solution pH, and ionic strength on the permeate flux (10–13). Bowen and Jenner (14) have comprehensively reviewed most of these earlier investigations. More recent studies on the influence of solute–solute interactions (14–18) are generally based on cell models (19, 20). Most of these studies assume a fixed structure for the concentration polarization layer while computing the interactions. Such a priori assumption of the solution structure may be reasonably accurate for systems where a cake layer has formed, but is inadequate for a disordered liquid-like system (21), typically represented by a concentration polarization layer.

The above limitation of the cell models may be overcome by employing rigorous statistical mechanical theories to relate the interparticle interactions to the structure of the solution (dispersion) (21–27). Contrary to the cell models that assume a fixed geometrical structure of the cake layer, the statistical mechanical approach allows the interparticle interactions to dictate the structure of the solution. This feature makes the approach amenable for studying the structure and thermodynamic properties of concentrated disordered systems.

A substantial theoretical development has been made in the understanding of sedimentation and gradient diffusion using statistical mechanical procedures (21–28). Noting that the dispersion microstructure evolves from the interparticle and hydrodynamic interactions in essentially the same manner during sedimentation and membrane filtration processes, the theory of batch sedimentation may be extended to predict permeate flux decline in membrane separation processes (25). However, the statistical mechanical theory of sedimentation is reasonably accurate only for dilute monodisperse suspensions of hard spherical particles (21). Till date there have been very limited studies on the influence of long-range interparticle colloidal interactions at higher solute particle concentrations based on this approach (27).

In this paper we apply the integral equation theory (29) to determine the equilibrium structure of the solution (dispersion) from the interparticle interactions. The Ornstein–Zernike (OZ) integral equation (30) is solved using the Percus–Yevick (PY) (31) and the hypernetted chain (HNC) (32) closures for a system of spherical particles to obtain the radial distribution function for the particulate species. A one-component particulate system interacting through either hard-sphere or Der-

jaguin–Landau–Verwey–Overbeek (DLVO) potential (33, 34) is considered. Theoretical estimates of the osmotic pressure, sedimentation coefficient, and diffusion coefficient are obtained from the interparticle interactions, solution structure, and hydrodynamic interactions based on the virial equation of state and the theory of batch sedimentation. Finally, the extent of concentration polarization and permeate flux decline is predicted by incorporating the concentration-dependent solution properties in the convective diffusion equation coupled with the osmotic pressure governed permeate flux equation. The theoretical approach is used to model the concentration polarization behavior (in absence of cake formation) during cross-flow membrane filtration of solute particles. A unique feature of the present approach is the establishment of a direct quantitative link between the interparticle interactions and the permeate flux decline behavior without assuming a structured solution in the polarized layer.

2. THEORETICAL BACKGROUND

In this section, we present the general theoretical outline for incorporation of interparticle interactions in a steady-state model of concentration polarization during cross-flow membrane filtration of charged solute particles. Typical solutions encountered in membrane filtration processes where concentration polarization is the primary cause of permeate flux decline (for instance, nanofiltration and ultrafiltration) involve a macrosolute, which may be a small colloidal particle or a macromolecule, a background electrolyte, and the solvent. The statistical mechanical treatment adopted in the study assumes the solution (dispersion) to be a pseudo-one-component system, where the macromolecular or colloidal particles (macrosolutes) are considered as monodisperse spherical particles suspended in a solvent continuum (35). Any microion in the system arising from dissociation of the background electrolyte is also considered to be a part of the continuum (35, 36). We use the terms “particle,” “colloid,” and “solute” interchangeably to indicate the particulate (macrosolute) species in the solution.

2.1. Mathematical Model of Concentration Polarization during Cross-flow Membrane Filtration

A typical cross-flow filtration process is shown schematically in Fig. 1, which depicts the physical and geometrical considerations for the mathematical treatment adopted in this section. The steady-state differential solute material balance in the polarized layer during cross-flow membrane filtration is written as

$$u \frac{\partial n}{\partial x} = \frac{\partial}{\partial y} \left(D(n) \frac{\partial n}{\partial y} \right) - v \frac{\partial n}{\partial y}, \quad [2.1]$$

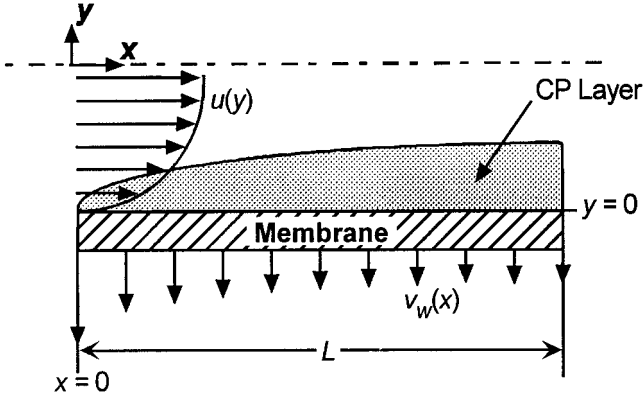


FIG. 1. Schematic representation of a cross-flow membrane filtration channel of length L depicting a steady state concentration polarization (CP) layer on the membrane surface. The axial (cross-flow) velocity u varies with the transverse (y direction) distance from the membrane surface. Within the confines of the polarized layer thickness, this velocity profile is assumed to be linear. The thickness of the CP layer increases, while the local permeate flux v_w decreases, with the axial (x direction) distance. The geometrical considerations depicted above are used to develop the mathematical model of CP and permeate flux decline in Section 2.1.

with the boundary conditions given by

$$n = n_b \quad \text{as } y \rightarrow \infty \quad [2.2]$$

and

$$v(n_m - n_p) = D(n_m) \left. \frac{\partial n}{\partial y} \right|_{y=0} \quad \text{at the membrane surface } (y = 0). \quad [2.3]$$

Here, n is the solute concentration (number density), u is the cross-flow velocity parallel to the membrane (along x), and $D(n)$ is the concentration dependent mutual diffusion coefficient of the solute. The subscripts b, m, and p represent the bulk solution, the membrane surface, and the permeate, respectively. The solvent velocity normal to the membrane (along y direction) in the polarized layer, v , is considered equal to the permeate velocity through the membrane v_w , and is expressed as

$$v_w = -v = \frac{\Delta P - \sigma_o \Delta \Pi_m}{\mu R_m}, \quad [2.4]$$

where ΔP is the applied pressure difference across the membrane, $\Delta \Pi_m (= \Pi_m - \Pi_p)$ is the osmotic pressure difference across the membrane, σ_o is the osmotic reflection coefficient, μ is the solvent viscosity, and R_m is the membrane resistance. The osmotic pressure difference across the membrane, which is a complex nonlinear function of the solute concentration, relates the membrane surface concentration and the permeate

flux. Note that the permeate flux v_w , the membrane surface concentration of the solute particles n_m , and the osmotic pressure difference across the membrane $\Delta \Pi_m$ are local quantities which vary with the axial position along the membrane channel. The osmotic reflection coefficient σ_o in Eq. [2.4] equals 1 for perfectly semipermeable membranes (solute rejection = 1).

In the above model, the diffusion coefficient D in Eq. [2.1] and the osmotic pressure difference $\Delta \Pi_m$ in Eq. [2.4] reflect the hydrodynamic and thermodynamic properties of the solution. While the osmotic pressure is a purely thermodynamic entity, the diffusivity reflects the interplay between thermodynamic and hydrodynamic interactions. A closer inspection of osmotic pressure and diffusivity in a microscopic scale provides a clearer perception of the influence of interparticle interactions on the permeate flux decline behavior.

2.2. Relationship between Macroscopic Solution Properties and Interparticle Interactions

2.2.1. Osmotic pressure. The osmotic pressure can be related to the interparticle interactions and the solution structure by the virial equation of state (29),

$$\Pi = nkT - \frac{2}{3} \pi n^2 \int_0^\infty r^3 g(r) \frac{dE}{dr} dr, \quad [2.5]$$

where r is the radial position, k is the Boltzmann constant, T is the absolute temperature, and $g(r)$ is the radial distribution function, which represents the solution structure and evolves from the pair interaction potential $E(r)$. The radial distribution (or pair correlation) function is generally obtained from the interaction potential by a statistical mechanical method, like solution of the Ornstein–Zernike (OZ) integral equation (29, 30) or Monte Carlo (MC) simulations (37). The osmotic pressure can also be determined from the compressibility equation of state (29), which is considered to be more general than the virial equation of state. Both equations of state, however, should ideally provide the same osmotic pressure when the underlying statistical mechanical theory for evaluation of the pair correlation function is exact. This criterion is often used to determine the accuracy of a statistical mechanical theory.

In this paper, we use the integral equation method to obtain the radial distribution function of the solutes. The method involves solution of the OZ integral equation for the solute particles, written as (29)

$$h(r) = c(r) + n \int h(r')c(r-r')dr', \quad [2.6]$$

where $h(r) = g(r) - 1$ is the total correlation function and $c(r)$ is the direct correlation function. Equation [2.6] can be solved using appropriate closures, which relate the direct cor-

relation function to the interaction potentials between the solute particles (29). Use of different closures will be described in Sections 3 and 4. Equation [2.6], being a convolution integral, needs to be solved using Fourier transforms. For radially symmetric interaction potentials considered in this study, the solution of the OZ equation becomes facile since one-dimensional Fourier transforms can be used to solve the three-dimensional problem. The numerical technique for solving the OZ integral equation employed in this study is briefly outlined in Appendix A.

2.2.2. Gradient diffusion coefficient. An expression for the concentration dependence of diffusion coefficient can be readily obtained from the theory of batch sedimentation. The concentration dependence of D can be expressed by the generalized Stokes–Einstein diffusivity equation as (28)

$$D(\phi) = D_\infty K(\phi) \frac{d[\phi Z(\phi)]}{d\phi}, \quad [2.7]$$

where ϕ is the solute volume fraction ($=4\pi r_p^3 n/3$ for spherical solutes of radius r_p), $K(\phi)$ is the sedimentation coefficient (ratio of hindered to free settling velocities), $Z(\phi)$ is the osmotic compressibility ($=\Pi/nkT$), and D_∞ is the Stokes–Einstein diffusivity at infinite dilution ($=kT/6\pi\mu r_p$). It is apparent from Eq. [2.7] that knowledge of the osmotic compressibility is an essential prerequisite for theoretical evaluation of the diffusion coefficient. The osmotic compressibility reflects the thermodynamic aspect of diffusion. The hydrodynamic aspect of the property is embedded in the sedimentation coefficient. In the following, a brief summary of the theory relating the sedimentation coefficient to the intermolecular and hydrodynamic interactions is presented.

2.2.3. Sedimentation coefficient. The sedimentation coefficient is generally expressed as a function of the solute volume fraction by (25)

$$K(\phi) = (1 - \phi)^\alpha. \quad [2.8]$$

For dilute suspensions, the exponent α can be obtained from a first-order series expansion of the above expression,

$$K(\phi) = 1 - \alpha\phi + O(\phi^2), \quad [2.9]$$

where the coefficient α is expressed for a suspension of monodisperse spheres of radius r_p as (21, 25, 26)

$$\alpha = \left\{ 5 + 3 \int_2^\infty [1 - g_{ss'}] s ds - \int_2^\infty [A_{11} + A_{12} + 2(B_{11} + B_{12}) - 3(1 + 1/s)] g_{ss'} s^2 ds \right\}. \quad [2.10]$$

Here, s is the nondimensional separation distance (r/r_p) between the sphere centers. The pair correlation function $g_{ss'}(r)$ in Eq. [2.10] is given by the Boltzmann distribution for dilute suspensions,

$$g_{ss'}(r) = \exp\left(-\frac{E(r)}{kT}\right). \quad [2.11]$$

The coefficients A_{ij} and B_{ij} in Eq. [2.10] are obtained from the solution of Stokes' equation for the solvent flow past two interacting spheres. The terms used in this case are (25)

$$\begin{aligned} A_{11} &= 1 - \frac{60}{16s^4} \\ A_{12} &= \frac{3}{2s} - \frac{1}{s^3} \\ B_{11} &= 1 \\ B_{12} &= \frac{3}{4s} + \frac{1}{2s^3}. \end{aligned} \quad [2.12]$$

It should be noted that Eq. [2.12] represents the approximate far-field forms of the coefficients for hydrodynamic interaction between two equal spheres, and is, in principle, appropriate in the limit $\phi \rightarrow 0$.

Substitution of Eqs. [2.11] and [2.12] in Eq. [2.10] and evaluation of the integrals yields an estimate of α , which reflects the effects of the interparticle interactions as well as the hydrodynamic interactions on the sedimentation coefficient. Use of the Boltzmann distribution and the far-field form of the hydrodynamic coefficients, coupled with the use of first-order series expansion in Eq. [2.9], renders the theory valid only for dilute colloidal dispersions ($\phi \rightarrow 0$). Extension of this theory for higher solute volume fractions, where α itself is treated as a concentration (volume fraction)-dependent parameter, is discussed in Section 3.2.

Equations [2.5] and [2.8] relate two macroscopic properties of a solution (osmotic compressibility and sedimentation coefficient) with the interparticle and hydrodynamic interactions. Combining these two relations, we can obtain the concentration dependence of diffusivity from Eq. [2.7]. The concentration dependent diffusivity can be used in the convective diffusion Eq. [2.1] to predict the extent of concentration polarization and, consequently, the permeate flux decline. The entire theoretical approach described above provides a generalized procedure for prediction of concentration polarization and permeate flux decline for different types of solutes on the basis of information regarding the interparticle and hydrodynamic interactions. We now describe the application of this general theoretical framework for different types of interaction potentials between the solute particles. In Sections 3 and 4, application of the statistical mechanical approach to evaluate

the osmotic pressure and diffusivity is described for solute particles interacting via hard-sphere and long-range interaction potentials, respectively. In Section 5, these predictions of solution properties are used to obtain the permeate flux decline behavior during cross-flow membrane filtration.

3. SOLUTION PROPERTIES FOR HARD SPHERICAL SOLUTE PARTICLES

At the outset, it should be noted that hard-spherical systems have been studied in great detail, and most of the results presented in this section are well known. Therefore, the primary objective in this section is to provide a facile outline for the application of the theory, depicting how the different solution properties can be predicted from information regarding the solute–solute interactions using some well-known equations arising from statistical thermodynamics of hard-sphere molecules.

3.1. Osmotic Compressibility

As stated earlier, the first step toward the estimation of osmotic pressure is the determination of the radial distribution function $g(r)$ for a given interaction potential. For hard spherical molecules, the interaction potential is written as

$$\begin{aligned} E(r) &= \infty & (r \leq \sigma) \\ &= 0 & (r > \sigma), \end{aligned} \quad [3.1]$$

where σ is the molecular diameter ($=2r_p$). Using this interaction potential in the Ornstein–Zernike (OZ) integral equation along with an appropriate closure yields the pair correlation function.

For hard-sphere interactions, the OZ integral Eq. [2.6] can be solved analytically along with the Percus–Yevick (PY) closure (31), written as

$$c(r) = \exp[\gamma(r)] - \gamma(r) - 1, \quad [3.2]$$

where $\gamma(r) = h(r) - c(r)$. The resulting expression for $g(r)$, when substituted in the virial expression, Eq. [2.5], provides the osmotic compressibility, which is related to the solute volume fraction as (29)

$$Z(\phi) = \frac{\Pi}{nkT} = \frac{1 + 2\phi + 3\phi^2}{(1 - \phi)^2}. \quad [3.3]$$

Using the compressibility equation of state, a second expression for the osmotic compressibility can be obtained (29),

$$Z(\phi) = \frac{1 + \phi + \phi^2}{(1 - \phi)^3}. \quad [3.4]$$

For hard-sphere systems, however, a more accurate expression for the osmotic compressibility is available. This exact equation of state, known as the Carnahan–Starling equation, is given by (38)

$$Z(\phi) = \frac{1 + \phi + \phi^2 - \phi^3}{(1 - \phi)^3}. \quad [3.5]$$

Equation [3.5] can also be obtained by mixing Eqs. [3.3] and [3.4] with weights $\frac{1}{3}$ and $\frac{2}{3}$, respectively (29).

The comparison of the three equations of state for hard-sphere systems given by Eqs. [3.3]–[3.5] is generally available in statistical mechanics texts (29). While Eq. [3.5] accurately predicts the osmotic compressibility of hard-sphere systems, Eqs. [3.3] and [3.4] slightly underpredict and overpredict the compressibility, respectively, at high solute volume fractions ($>ca. 0.35$). At low solute volume fractions, however, the three expressions yield nearly identical results. Furthermore, the PY-compressibility expression [3.4] is remarkably close to the Carnahan–Starling equation [3.5] even at high volume fractions. Based on the above observations, the PY-compressibility equation can, in principle, be used to predict the osmotic pressure to a reasonably good approximation. In this study, however, we resort to the Carnahan–Starling equation of state [3.5] for hard-sphere systems, as it is known to be exact.

3.2. Sedimentation Coefficient

3.2.1. Existing techniques. Evaluation of the sedimentation coefficient follows the determination of the exponent α in Eq. [2.8]. Substitution of Eq. [3.1] in Eq. [2.11] and evaluation of the integrals in Eq. [2.10] leads to an estimate of this parameter for hard-sphere interactions. The procedure yields a value of 6.875 for α . A more precise value for the parameter, 6.55, was obtained by Batchelor (21). Using this second value of the exponent in Eq. [2.8] we obtain

$$K(\phi) = (1 - \phi)^{6.55}. \quad [3.6]$$

It is well known that the volume fraction dependence of the sedimentation coefficient given by Eq. [3.6] is remarkably accurate for dilute monodisperse hard-spherical systems (25, 39). Empirical correlations for the volume fraction dependence of sedimentation coefficient involving different values of the exponent in Eq. [2.8] are also common (25, 40, 41).

A second expression for the sedimentation coefficient of hard spherical particles is obtained using the Happel cell model (19),

$$K(\phi) = \frac{1 - 1.5\phi^{1/3} + 1.5\phi^{5/3} - \phi^2}{1 + 0.667\phi^{5/3}}. \quad [3.7]$$

The Happel cell model is considered to be accurate for mod-

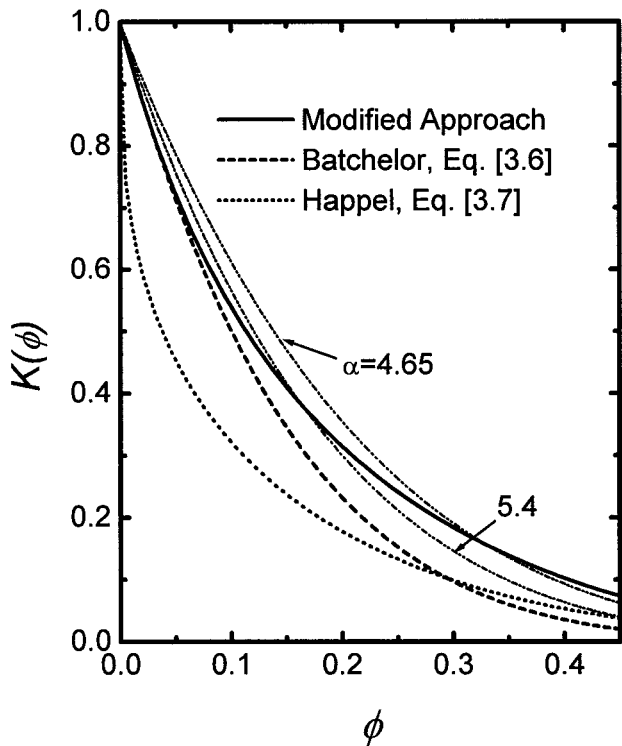


FIG. 2. Variation of the sedimentation coefficient with solute volume fraction for hard spherical particles obtained using different theoretical approaches. The solid line is obtained using the modified technique described in Section 3.2.2, the dashed line is obtained using a constant coefficient $\alpha = 6.55$ in Eq. [3.6], and the dotted line is obtained using Happel's cell model, Eq. [3.7]. The two curves corresponding to $\alpha = 4.65$ and 5.4 represent the empirical fits of Eq. [2.8] to the experimental sedimentation coefficient data reported in (40, 41).

erate to high solute volume fractions (19, 20), and hence, Eq. [3.7] is expected to yield the correct asymptotic limit for the sedimentation coefficient at high solute volume fractions (near the close packing densities for hard-sphere molecules).

Figure 2 depicts the variation of the sedimentation coefficient with solute volume fraction obtained using Eqs. [3.6] (dashed line) and [3.7] (dotted line). In dilute suspensions, Eq. [3.6] yields larger values of the sedimentation coefficient than Happel's expression. Furthermore, Eq. [3.6] predicts a linear variation of the sedimentation coefficient with solute volume fraction as $\phi \rightarrow 0$. Happel's expression, Eq. [3.7], on the other hand, predicts that the sedimentation coefficient depends on $\phi^{1/3}$ in this limit (20). This is a major argument in favor of Eq. [3.6] in dilute systems, as most experimental observations depict a linear decay of the sedimentation coefficient with solute volume fraction in dilute colloidal dispersions (21, 25, 40, 41). At higher volume fractions ($\phi > 0.3$), however, Eq. [3.7] predicts larger values of the sedimentation coefficient than Eq. [3.6], and is closer to experimental observations (40, 41). Assuming that Eqs. [3.6] and [3.7] provide the correct asymptotic limits in dilute and concentrated solutions, respectively, Fig. 2 suggests that these two expressions may be

combined to provide the sedimentation behavior of hard-sphere solutes over a wide concentration range.

3.2.2. Modified theory of sedimentation. The combination of the two estimates of sedimentation coefficient is, however, quite empirical, and poses problems regarding the selection of an appropriate value of ϕ where the transition from Eq. [3.6] to Eq. [3.7] should be made. It should also be noted that Eq. [3.6] is more appropriate for disordered liquid-like systems owing to its use of arbitrary solution structure (21). In this respect, it is worthwhile to explore the application of Eq. [2.8] to more concentrated systems using the actual radial distribution function of a concentrated solution obtained from the OZ integral equation (21–23, 27).

The expression for the parameter α , Eq. [2.10], contains the pair correlation function $g(r)$, which is related to the solution structure at a given concentration. In the dilute limit, $g(r)$ is evaluated using the Boltzmann distribution $g_{ss}(r)$, Eq. [2.11]. At higher solute concentrations, however, the OZ integral equation described in Section 2 can be utilized to evaluate the pair correlation function based on pairwise summation of many body interactions. As the pair correlation function obtained using this procedure depends on solute concentration, incorporation of this $g(r)$ in the integrals in Eq. [2.10] renders the parameter α concentration dependent. The above modification is applicable if the solution structure is solely determined by the interparticle interactions, and the hydrodynamic interactions do not disturb this structure (22, 42).

The fact that the hydrodynamic interactions do not significantly modify the solution structure in the concentration polarization (CP) layer during cross-flow filtration can be verified from the local Peclet number attained in these processes. Denoting the local shear rate as $\dot{\gamma}$, the local Peclet number ($Pe = 6\pi\mu\dot{\gamma}r_p^3/kT$) in the CP layer rarely attains values >0.01 for $\dot{\gamma} < 2000 \text{ s}^{-1}$ and $r_p \leq 10 \text{ nm}$. Since the Peclet number is substantially smaller than 1, the influence of hydrodynamic interactions on the solution structure can be safely ignored during typical concentration polarization phenomena discussed in this study.

An implementation of the modified approach for prediction of sedimentation coefficient involves solution of the OZ integral equation with the PY closure for hard-spherical solutes to evaluate the pair correlation function, followed by its substitution in Eq. [2.10] to evaluate α . The procedure yields different values of α at different solute volume fractions. The integrals in Eq. [2.10] can be evaluated numerically over the radial distances at which $g(r)$ is not 1 (that is, over $2 < r < r_{\max}$) and analytically at larger distances ($r_{\max} < r < \infty$) at which $g(r) \approx 1$. Here r_{\max} is the maximum radial distance used in the numerical solution of the OZ equation.

The resulting variation of the sedimentation coefficient for hard spherical particles obtained using the concentration dependent α in Eq. [2.8] is shown as the solid line in Fig. 2. Also plotted in Fig. 2 are two empirical curves obtained using $\alpha =$

4.65 and 5.4 in Eq. [2.8]. These empirical curves were obtained from best fits of Eq. [2.8] to the experimental sedimentation coefficients of silica spheres ($r_p = 71$ and 35 nm) (41) and polystyrene latex particles ($r_p = 1.55$ μm) (40), respectively. It is evident that the estimate of $K(\phi)$ obtained using the modified approach is much closer to these curves than either Eq. [3.6] or [3.7] at larger volume fractions ($0.1 < \phi < 0.45$). The volume fraction dependence of $K(\phi)$ predicted by the modified approach appears to be in excellent agreement with experimental observations over the entire range of volume fraction ($\phi < 0.45$) for hard-spherical colloids (25, 40, 41). Notably, earlier approaches for prediction of sedimentation coefficient resort to a single constant value of α to fit the entire range of experimental observations (21, 22, 25, 39). In the present approach, α itself varies with concentration, generally ranging between about 6.875 in dilute solutions ($\phi \rightarrow 0$) to a value of ca. 4.5 in concentrated solutions.

It is important to note that the modification of the pair correlation function in Eq. [2.10] merely attempts to substitute a more accurate structure of the solution to improve the accuracy of α at a given solute concentration. Despite the use of the more accurate $g(r)$, Eq. [2.10] should still be strictly valid for dilute systems as we have not incorporated the near field hydrodynamic interactions in the present approach. However, it is indeed gratifying that a simple substitution of an accurate solution structure alone provides such a dramatic improvement in the sedimentation coefficient predictions at high solute volume fractions.

3.3. Gradient Diffusion Coefficient

Substitution of the osmotic compressibility and the sedimentation coefficient in Eq. [2.7] yields the volume fraction dependence of the diffusion coefficient. Based on Eq. [3.5] for $Z(\phi)$ of hard-spherical particles, the expression for the concentration dependent diffusivity is

$$D(\phi) = D_\infty K(\phi) \frac{(1 + 4\phi + 4\phi^2 - 4\phi^3 + \phi^4)}{(1 - \phi)^4}. \quad [3.8]$$

Figure 3 depicts the variation of the scaled gradient diffusion coefficient (D/D_∞) with particle volume fraction obtained using Eq. [3.6] with $\alpha = 6.55$ (dashed line), Eq. [3.7] (dotted line), and the modified approach (solid line) for evaluating $K(\phi)$ in Eq. [3.8]. The diffusivity for hard spheres obtained using Eq. [3.6] first increases and then decreases with a further increase in volume fraction. The increase in the gradient diffusion coefficient with volume fraction has been experimentally observed in the dilute limit (43, 44). However, the subsequent decrease at large volume fractions has not been experimentally corroborated. Experimental observations generally indicate a monotonic rise in the gradient diffusion coefficient with solute volume fraction. Consequently, the predictions of diffusivity based on Eq. [3.6] are questionable for high

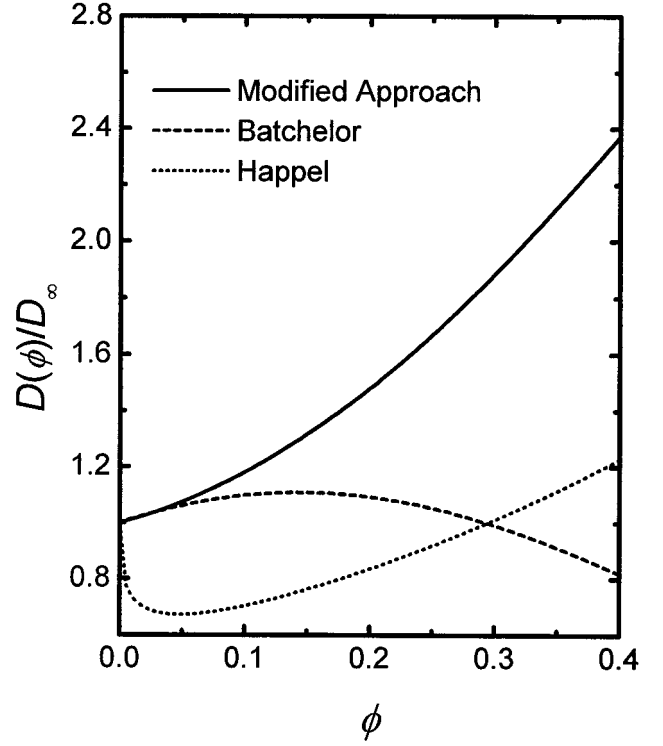


FIG. 3. Dependence of the gradient diffusion coefficient on solute volume fraction for hard spherical particles obtained using different theoretical estimates of the sedimentation coefficient based on the modified approach, Eq. [3.6], and Eq. [3.7] (Fig. 2) in Eq. [3.8].

solute volume fractions. Indeed, such a deviation is consistent with the fact that the underlying theory for sedimentation is valid only for dilute systems.

The concentration dependence of diffusivity obtained using Happel's expression, Eq. [3.7], in Eq. [3.8] is in sharp contrast to that observed using Eq. [3.6]. While this expression results in quite unrealistic behavior at low volume fractions, the predictions indicate an increase in diffusivity with particle concentration for higher volume fractions.

The modified approach (solid line), on the other hand, predicts a monotonic increase in the gradient diffusion coefficient with solute volume fraction. It is worth noting that the diffusion coefficient evaluated using this approach is a significant improvement over both existing approaches based on Batchelor's and Happel's models. While the approach conforms to the dilute limit predictions of Batchelor's expression, Eq. [3.6], it also predicts a monotonic increase in the diffusivity up to quite high volume fractions. Further evidence for the validity of the modified approach at higher volume fractions is presented in Section 4, where the predicted variations of the diffusion coefficient are compared with experimental results available in the literature.

It should be noted that theoretical prediction of the concentration dependence of D is a formidable task, as a small error in the evaluation of $K(\phi)$ can lead to a drastic alteration in the

predicted values. Thus, while the modified approach provides more accurate results for $K(\phi)$, it should be treated carefully at higher solute particle concentrations. A limitation of the modified theory of sedimentation presented here lies in the use of far field expressions for the hydrodynamic interaction parameters given by Eq. [2.12]. At high volume fractions, these expressions should be appropriately modified to account for the dominance of the near field hydrodynamic interactions (23, 25) in the integrals in Eq. [2.10]. In very dilute systems exhibiting repulsive interactions, however, the consideration of far-field hydrodynamic interactions should be adequate, as the distance between the solute particles is considerably larger.

4. SOLUTION PROPERTIES FOR CHARGED SOLUTE PARTICLES

In this section, the concentration dependence of the osmotic compressibility and the gradient diffusion coefficient are determined for charged solute particles with long-range DLVO interactions. The procedure for the evaluation of these properties is essentially similar to that employed for hard-spherical molecules, except for the consideration of a more complex form of colloidal interaction between the solute particles.

4.1. Long-Range DLVO Interaction Potential

The interaction between two charged solute particles is generally expressed by the DLVO potential, which comprises an attractive Lifshitz–van der Waals (VDW) and a repulsive electrostatic double layer (EDL) interaction (45). The resulting expression for two spherical particles of diameter σ , separated by a dimensionless center to center distance $R(=r/\sigma)$, is given by (35, 46)

$$E(r) = -\frac{A}{12} \left[\frac{1}{R^2} + \frac{1}{R^2 - 1} + 2 \ln \left(1 - \frac{1}{R^2} \right) \right] + \frac{z_p^2 e^2}{4\pi\epsilon_0\epsilon_r} \frac{\exp[-\kappa(r - \sigma)]}{r(1 + \kappa\sigma/2)^2}, \quad [4.1]$$

where A is the Hamaker constant, z_p is the charge number on the solute particle, e is the electronic charge, ϵ_0 is the dielectric permittivity of vacuum, ϵ_r is the dielectric constant of the solvent, and κ is the inverse Debye screening length. The first term in Eq. [4.1] represents the VDW component of the interaction, while the second term represents the screened EDL interaction between the charged particles. It may be noted that the VDW interaction energy diverges at contact ($R = 1$). To prevent this divergence, a cut-off separation distance of 0.158 nm was used in Eq. [4.1] (45). A hard-spherical repulsion was assumed at separation distances lower than this value.

Three parameters in Eq. [4.1] completely characterize the interparticle colloidal interactions, namely, the effective Hamaker constant A , the charge on the particle z_p , and the Debye

screening length κ^{-1} . These three parameters may be determined independently. Theoretical estimates of the Hamaker constant may be obtained from the polarizability of the various species (45, 46). The particle charge can be determined experimentally by acid–base titration or can be estimated from electrokinetic potentials obtained from electrophoretic mobility measurements (45). The Debye screening length of the electrostatic interactions for a symmetric ($z:z$) background electrolyte can be determined from (25)

$$\kappa^{-1} = \left(\frac{\epsilon_0\epsilon_r kT}{2 \times 10^3 N_A e^2 z^2 C_{EL}} \right)^{1/2}, \quad [4.2]$$

where N_A is the Avogadro number and C_{EL} is the molar concentration of the background electrolyte. The screening length becomes smaller at high electrolyte concentrations, signifying that the electrostatic interactions become short ranged in such situations.

4.2. Determination of Solution Structure and Properties

4.2.1. Osmotic compressibility. Using the interaction potential described by Eq. [4.1], the radial distribution function $g(r)$ is determined by solving the OZ integral Eq. [2.6] along with the hypernetted chain (HNC) closure (29, 32),

$$c(r) = \exp[-\beta E(r) + \gamma(r)] - \gamma(r) - 1, \quad [4.3]$$

where $\gamma(r) = h(r) - c(r)$ and $\beta = 1/kT$.

Substitution of the radial distribution function and the interaction potential in Eq. [2.5] yields the osmotic compressibility Z . The variation of Z with the solute volume fraction for different particle surface charges and electrolyte concentrations is shown in Fig. 4. The calculations of the osmotic compressibility were performed for the parameters shown in Table I. Increasing the charge and decreasing the electrolyte concentration substantially increases the osmotic compressibility from the hard-sphere compressibility. When the particle charge is small, the compressibility may be lower than the hard-sphere values at high electrolyte concentrations owing to the screening of the electrostatic repulsion and the predominance of the van der Waals attraction. This behavior is depicted in Fig. 4, where the compressibility for a particle charge number $z_p = -10$ and electrolyte concentration $C_{EL} = 0.1$ M falls below the hard-sphere compressibility.

The remarkable accuracy of the theoretical predictions is evident from Fig. 5, where the predictions are compared with experimental osmotic pressure data for aqueous saline BSA at an electrolyte (1:1) concentration of 0.15 M obtained by Vilker *et al.* (46). All the parameters used in the calculations were similar to those reported in that study and are nearly identical to those reported in Table I. The results indicate that the OZ integral equation approach can reliably predict the osmotic

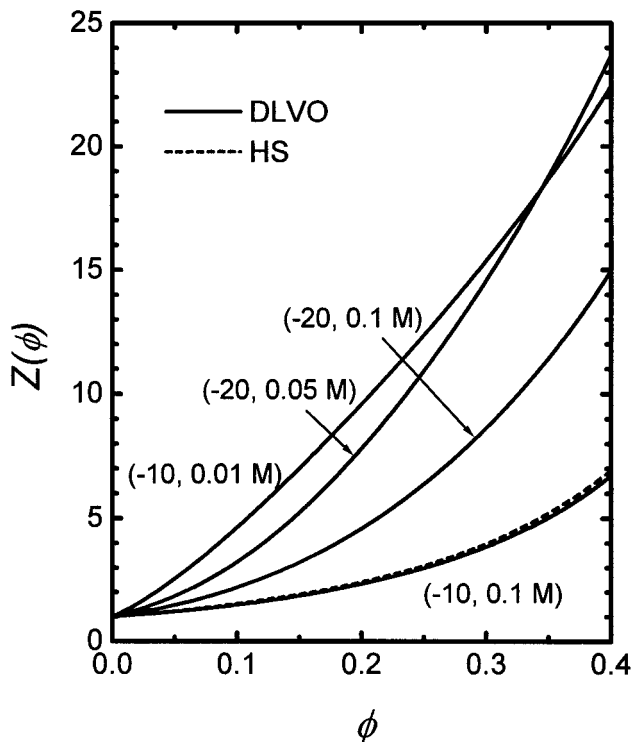


FIG. 4. Variation of the osmotic compressibility with volume fraction for charged particles interacting through DLVO potential. The solid lines were obtained for different combinations of particle charge z_p and molar electrolyte concentration C_{EL} , respectively, represented by the numbers within parentheses accompanying each curve. Other conditions used in the calculations are given in Table I. The dashed curve was obtained for hard-sphere (HS) interactions.

pressure of macromolecular systems based on the DLVO interaction potential.

4.2.2. Sedimentation coefficient. The sedimentation coefficient of a dilute dispersion of solute particles can be determined from Eq. [2.8] if the parameter α is known. Substituting the DLVO potential [4.1] in Eq. [2.11] yields the Boltzmann distribution function $g_{ss}(r)$, which is then used in Eq. [2.10] to obtain α . Figure 6 depicts the sedimentation coefficients ob-

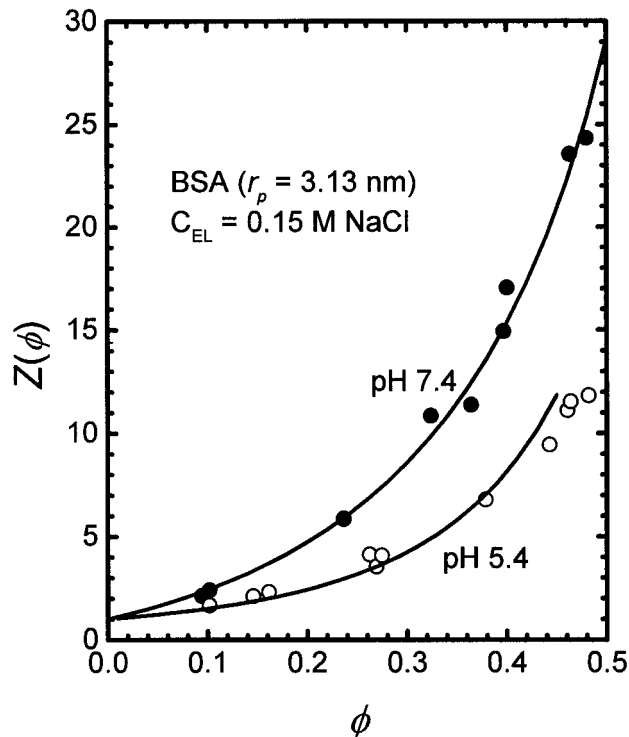


FIG. 5. Comparison of the theoretical predictions of the osmotic compressibility of bovine serum albumin (BSA) obtained using the HNC integral equation theory with experimental observations of Vilker *et al.* (46). The theoretical calculations were performed assuming an equivalent spherical radius of the particles to be 3.13 nm. The particle charge numbers were -20.4 and -9.1 , respectively, at pH 7.4 and 5.4. All other parameters used in the calculations are same as in Table I.

TABLE I

Parameters Used for Prediction of the Solution Properties

Solute radius, r_p (nm)	3.0
Charge number on particle, z_p (-)	-10 and -20
Electrolyte (1:1) concentration, C_{EL} (M)	0.1, 0.05, and 0.01
Hamaker constant, A (J)	1.65×10^{-21}
Solute volume fraction, ϕ (-)	0 - 0.4
Minimum equilibrium cut-off distance, d_0 (nm) ^a	0.158
Solvent dielectric constant, ϵ_r (-)	78.54
Temperature, T (K)	298

^a The minimum equilibrium cut-off distance is employed to prevent the divergence of the attractive (VDW) component of the DLVO interaction energy at contact (45).

tained using this procedure (solid lines). The sedimentation coefficient for hard-sphere solutes, obtained using Batchelor's expression is also shown as dashed lines in the figure. It is evident that by increasing the mutual repulsion between the colloidal particles (by increasing the charge or lowering the electrolyte concentration), the sedimentation coefficient can be substantially decreased from the hard-sphere values. It is, however, worth noting that experimental observations of the sedimentation coefficient for charged particles at higher solute volume fractions are much larger than those predicted by the solid lines and generally do not deviate significantly from the sedimentation coefficient of hard spherical particles (40). This leads us to believe that the estimates of $K(\phi)$ for charged particles progressively deteriorate at higher solute concentrations and for long-range interactions (for instance, at low electrolyte concentrations), which invalidate the use of Boltzmann distribution, Eq. [2.11]. Use of this $K(\phi)$ to evaluate the diffusion coefficient results in unrealistic predictions at high solute concentrations. Happel's expression for $K(\phi)$, Eq. [3.7] (dotted line), on the other hand, is known to be more appropriate at larger solute concentrations. Using these two observations, the dilute limit result for $K(\phi)$ may be combined with

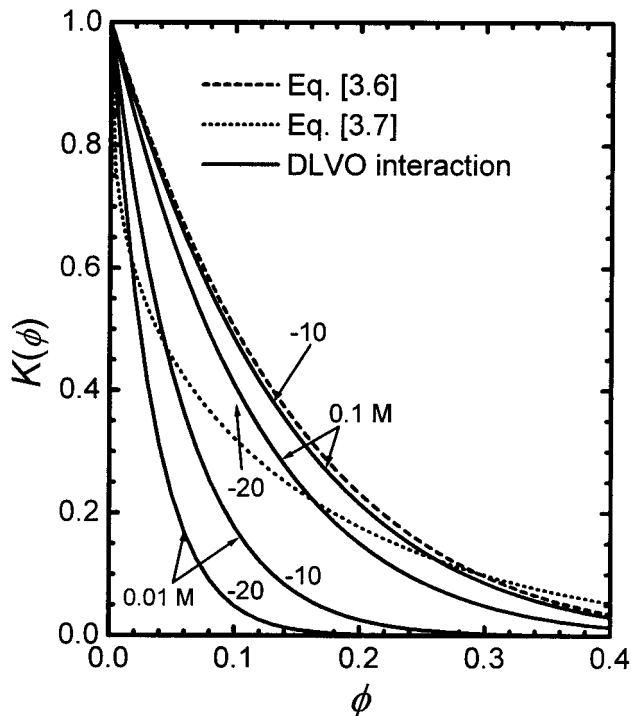


FIG. 6. Variation of the sedimentation coefficient with volume fraction obtained for different particle charges and electrolyte concentrations using available theoretical approaches. The solid lines were obtained using fixed values of α evaluated from Eq. [2.10] using the DLVO interaction potential in the Boltzmann distribution function, Eq. [2.11]. The dashed and dotted lines were obtained for hard-sphere particles using Eq. [3.6] and [3.7], respectively. The DLVO interaction energy was calculated using the parameters listed in Table I.

Happel's expression for higher solute concentrations, as suggested in Section 3.2.

In this study, however, we circumvent this empirical method by employing the pair correlation function obtained from the solution of the HNC integral equation in Eq. [2.10]. This modified procedure yields the concentration dependence of α , which, in turn, is used in Eq. [2.8] to predict the concentration dependence of K . The sedimentation coefficients predicted by this procedure are depicted in Fig. 7. It is evident from the figure that the sedimentation coefficient becomes independent of the particle charge and screening length at high solute volume fractions. Under such conditions, the sedimentation coefficient of charged colloidal particles resembles the hard-sphere sedimentation coefficient. The influence of long-range colloidal interactions on the sedimentation coefficient is apparent only in dilute solutions.

The above behavior of the sedimentation coefficient is consistent with the observation that a system of particles interacting through a screened Coulomb potential assumes a nearly hard spherical structure at high solute volume fractions (35). Figure 8 shows the pair correlation functions obtained from the solution of the OZ integral equation for hard-spherical and charged solute particles at high (Fig. 8a) and low (Fig. 8b)

volume fractions. The two pair correlation functions (solid and dashed lines) are quite identical at high solute concentrations, although they are obtained on the basis of different interaction potentials and closure equations. This similarity becomes more obvious when we note that, at lower solute volume fractions, the pair correlation functions obtained using the two potentials are considerably different, as shown in Fig. 8b.

4.2.3. Gradient diffusion coefficient. The dependence of the diffusivity on solute volume fraction can be obtained by substituting the osmotic compressibility and the sedimentation coefficient in the generalized Stokes–Einstein Eq. [2.7]. The calculation of the diffusivity was performed numerically using the sedimentation coefficient and the osmotic compressibility data. These numerical estimates of the diffusion coefficient were then correlated using a polynomial of the form

$$\frac{D(\phi)}{D_\infty} = 1 + a_1\phi + a_2\phi^2 + a_3\phi^3 + a_4\phi^4 + \dots, \quad [4.4]$$

where the coefficients a_i were determined using a simple regression analysis of the numerical data.

Figure 9 shows the variation of the diffusion coefficient with ϕ predicted for different solute particle charge numbers and

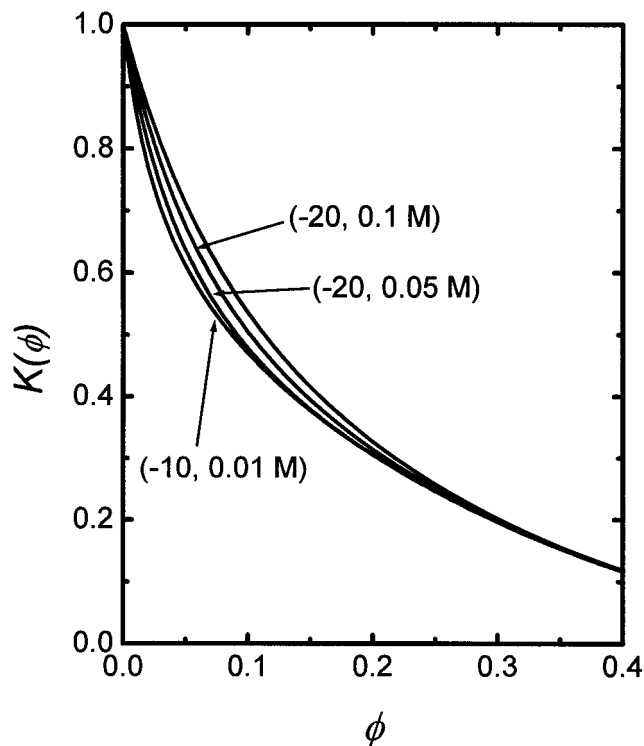


FIG. 7. Variation of the sedimentation coefficient with volume fraction for different combinations of particle charge and electrolyte concentration (shown in parentheses) obtained using the modified technique for evaluation of sedimentation coefficient employing the $g(r)$ determined from the HNC integral equation.

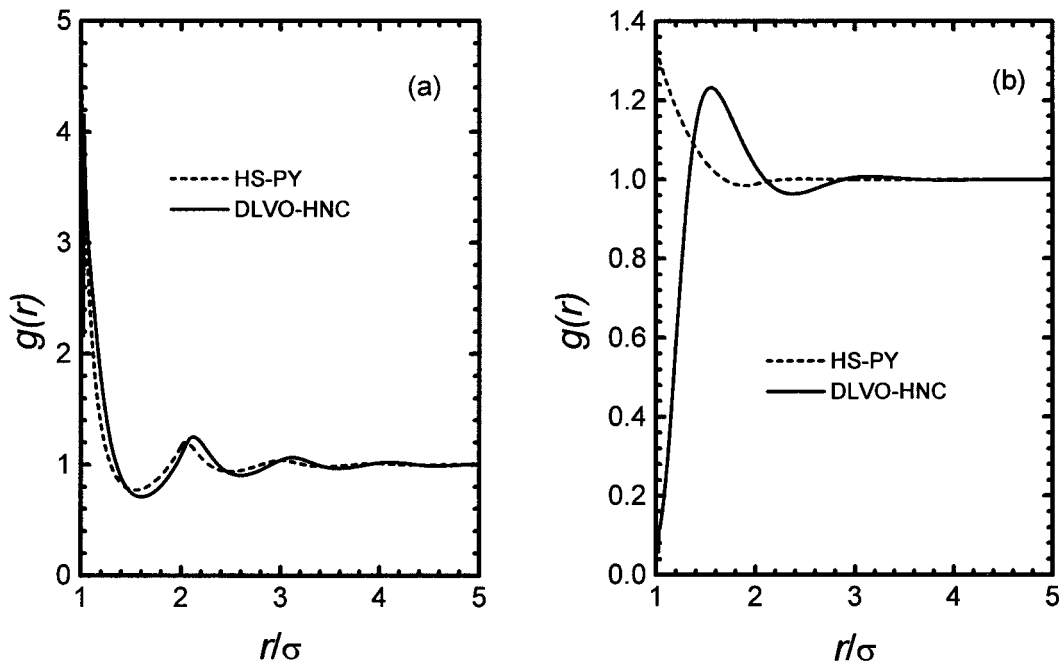


FIG. 8. Comparison of the pair correlation functions for hard-sphere and charged particles at (a) high solute volume fraction ($\phi = 0.4$) and (b) low solute volume fraction ($\phi = 0.05$). The solid line was obtained using the HNC integral equation, while the dashed line was obtained using the PY integral equation. The solid line was obtained using the conditions in Table I for a particle charge of -10 and an electrolyte concentration of 0.01 M.

electrolyte concentrations. While the solid lines represent the predictions based on the modified approach, the dashed line was obtained using the theoretical approach of Batchelor (21, 28) for hard-sphere particles. In dilute systems, the diffusion coefficient increases almost linearly with solute volume fraction for high charges and low electrolyte concentrations. At lower electrolyte concentrations, the rise in $D(\phi)$ is phenomenal, often showing a five- to sevenfold increase compared to the Stokes–Einstein diffusivity. The rise in diffusivity for charged solute particles at low electrolyte concentrations is in qualitative agreement with the experimental results of Anderson *et al.* (43), who observed a linear rise in diffusivity of BSA with volume fraction. These observations, however, were made for very low BSA concentrations and, therefore, do not lend any insight to the behavior at higher volume fractions.

Experimental observations of the concentration dependence of diffusivity were made over a wider concentration range at high electrolyte concentrations by Phillis *et al.* (44). These experimental values for the diffusion coefficient of BSA are compared with theoretical predictions based on the modified approach in Fig. 10. The experimental observations were reported for a pH range of 7.2 to 7.6 and a background electrolyte concentration of 0.15 M NaCl. These conditions closely emulated a system of hard spherical particles with a short-range electrostatic repulsion. This is evident from the close correspondence between the theoretical predictions for the hard spherical particles (dashed line) and the experimental data. The solid curve was obtained by assuming the equivalent spherical radius of the particles to be 3.13 nm and the particle charge

number to be -20.4 (corresponding to pH 7.4) (46). These predictions are in good agreement with the experimental data for $\phi < 0.1$. However, since the BSA molecules are not spherical (46) (contrary to the theoretical assumption) and the use of Debye screening parameter is questionable at high particle volume fractions (35), it is difficult to assess the accuracy of the theoretical predictions based on DLVO interaction for $\phi > 0.1$. Despite this, it is indeed significant that most of the experimental points in Fig. 10 are closely bounded by the predictions of the modified approach (solid and dashed lines). In sharp contrast, the concentration dependence of diffusivity obtained using the sedimentation coefficient expression of Batchelor, Eq. [3.6] (dotted line), differs markedly from the experimental results. It is clearly evident that use of the Boltzmann distribution function to predict $K(\phi)$ leads to a grossly erroneous prediction of the diffusion coefficient at high solute volume fractions.

Based on the above predictions, it becomes clear that variations of diffusivity with solute concentration and the physicochemical properties of the solution cannot be ignored when modeling the concentration polarization during membrane filtration, as this can seriously affect the prediction of the extent of concentration polarization. In a typical concentration polarization layer formed during cross-flow filtration of small colloidal particles or macromolecules, the solute particle concentration is expected to vary over the range considered in our study (volume fractions up to *ca.* 0.4). Over this concentration range, the diffusion coefficient can vary significantly, thereby altering the diffusive transport term in the convective-diffusion

equation. Such variations can reduce the extent of concentration polarization and, hence, result in higher permeate flux.

5. PREDICTION OF PERMEATE FLUX DURING CROSS-FLOW MEMBRANE FILTRATION

5.1. Flux Predictions Using the Variable-Diffusivity Concentration Polarization Model

Substitution of the gradient diffusion coefficient and the osmotic compressibility in Eqs. [2.1]–[2.4] and solving these using an appropriate numerical technique provide a coupled prediction of the extent of concentration polarization and permeate flux decline. The numerical technique for solving the steady state convective–diffusion Eq. [2.1] for variable (concentration-dependent) diffusivity is described in Appendix B.

In presenting the following results, the local permeate flux was scaled with respect to the pure solvent flux v_0 ($=\Delta P/\mu R_m$). Typical variations of the scaled permeate flux with dimensionless axial position (x/L) in the filtration channel are

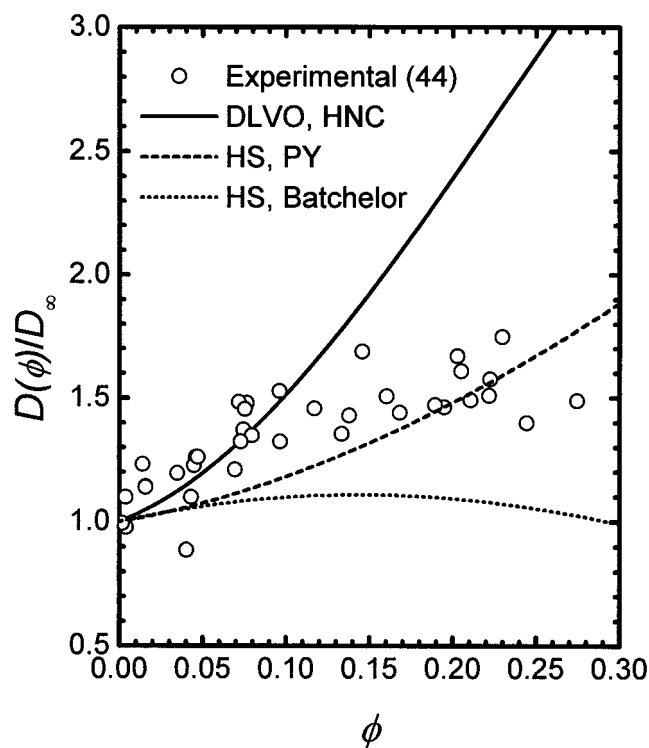


FIG. 10. Comparison of the various predictions of the concentration dependence of diffusion coefficient with the experimental diffusivity of BSA at a high electrolyte (1:1) concentration (0.15 M). The experimental data are taken from Phillis *et al.* (44). The solid and the dashed lines were obtained using the modified approach for prediction of sedimentation coefficient based on DLVO and hard-sphere interactions, respectively. The solid line was obtained using the radial distribution function determined from the HNC closure for a particle charge number of -20.4 and particle radius of 3.13 nm (46). The dashed line was obtained using the PY closure for hard-sphere interaction. The dotted line depicts the prediction for hard spherical particles using Batchelor's approach (25).

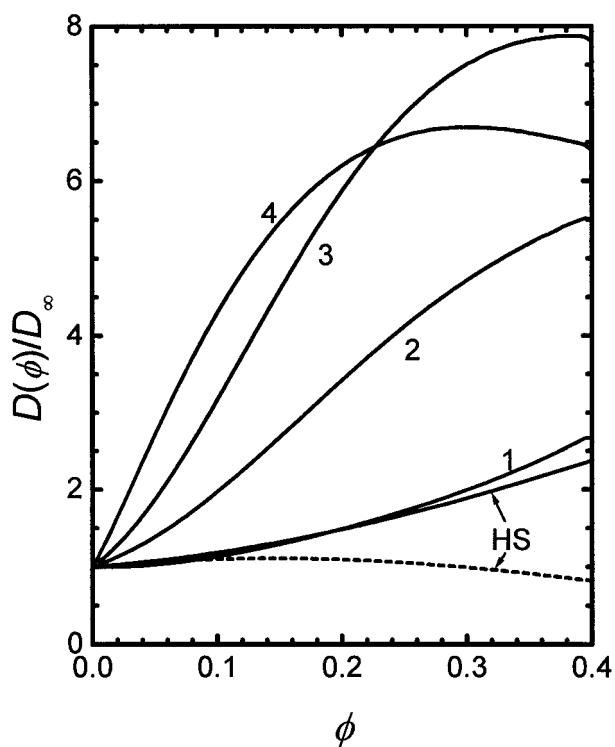


FIG. 9. Theoretical predictions of the variation of gradient diffusion coefficient with particle volume fraction. The solid lines were obtained using the modified approach for evaluating the sedimentation coefficient. While curves 1–4 were obtained for different combinations of particle charge and ionic strength (using HNC closure), the solid line marked “HS” was obtained for hard-sphere particles (using PY closure). The dashed line represents the diffusion coefficient for hard spherical particles obtained using Batchelor's approach (25). All parameters used in the calculations are shown in Table I. Curve 1, $z_p = -10$, $C_{EL} = 0.1$ M; curve 2, $z_p = -20$, $C_{EL} = 0.1$ M; curve 3, $z_p = -20$, $C_{EL} = 0.05$ M; curve 4, $z_p = -10$, $C_{EL} = 0.01$ M.

shown in Fig. 11. While the solid and dashed lines depict the scaled permeate flux for variable diffusivity, the dotted line (lowermost curve) represents the corresponding predictions obtained using a constant Stokes–Einstein diffusion coefficient in the model. The predictions for hard-spherical interactions were obtained using the Carnahan–Starling equation for osmotic pressure. The variation of diffusivity was obtained using Eq. [3.6] and the modified method for evaluation of $K(\phi)$ in Eq. [3.8]. While the lower dashed curve for hard-sphere interactions was obtained using Eq. [3.6], the upper dashed curve was obtained on the basis of the modified technique for evaluation of $K(\phi)$. The solid lines were obtained for various combinations of particle charge and electrolyte concentration, as indicated in the figure. All other conditions (pressure, feed bulk concentration, and cross-flow velocity) were kept constant during the calculations.

It is apparent from Fig. 11 that the present model is capable of predicting the local variations of the permeate flux in a cross-flow filtration channel for a wide range of physicochem-

ical conditions. Both particle charge and electrolyte concentration, which are manifested as variations of diffusivity and osmotic pressure, have a dramatic influence on the permeate flux. At low electrolyte concentrations or for highly charged particles, the permeate flux predicted by the variable-diffusivity model becomes significantly higher than the corresponding predictions using the constant diffusivity model. This implies that the constant diffusivity model of concentration polarization can significantly underpredict the permeate flux during cross-flow membrane filtration of charged solute particles.

5.2. Dependence of Permeate Flux on Ionic Strength and Particle Charge

It was shown in Fig. 11 that the permeate flux decline predicted by considering the concentration dependence of diffusivity is less severe than that observed using a constant diffusivity in the concentration polarization model. Use of a constant diffusion coefficient in the convective–diffusion

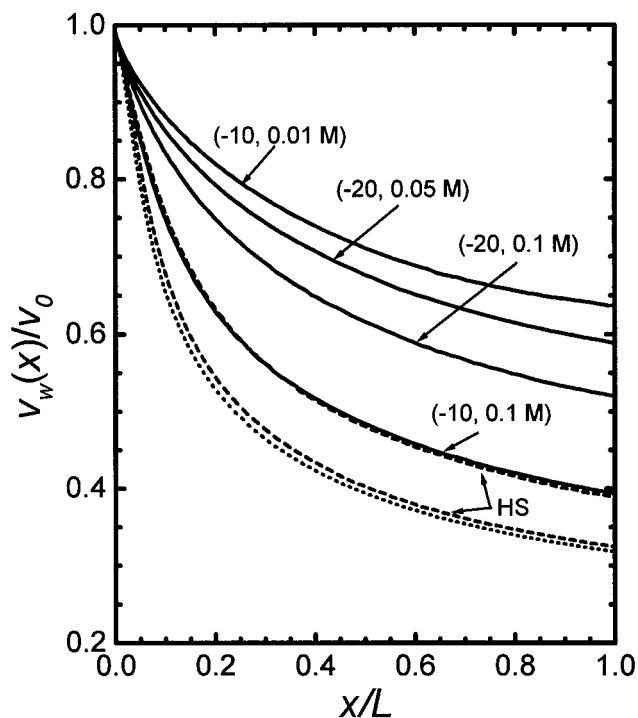


FIG. 11. Variation of the scaled permeate flux with scaled axial position in the filtration channel obtained using different estimates of the solution properties. The solid lines were obtained using the DLVO interaction potential for the particle charge and electrolyte (1:1) concentrations indicated in parentheses. The upper dashed line was obtained using the modified estimate of the sedimentation coefficient in Eq. [3.8] to predict the concentration dependence of diffusivity for hard-sphere molecules. The lower dashed line was obtained using Eq. [3.6] in Eq. [3.8]. The dotted line was obtained using a constant Stokes–Einstein diffusivity in the convective diffusion equation. The operating conditions for which the predictions were obtained are $\Delta P = 200$ kPa, $\dot{\gamma} = 100$ s $^{-1}$, $r_p = 3$ nm, and $\phi_b = 0.01$. The length of the filtration channel was 0.5 m. The pure water permeability of the membrane, $(\mu R_m)^{-1}$ was 6.0×10^{-11} m Pa $^{-1}$ s $^{-1}$. Other solute properties are listed in Table I.

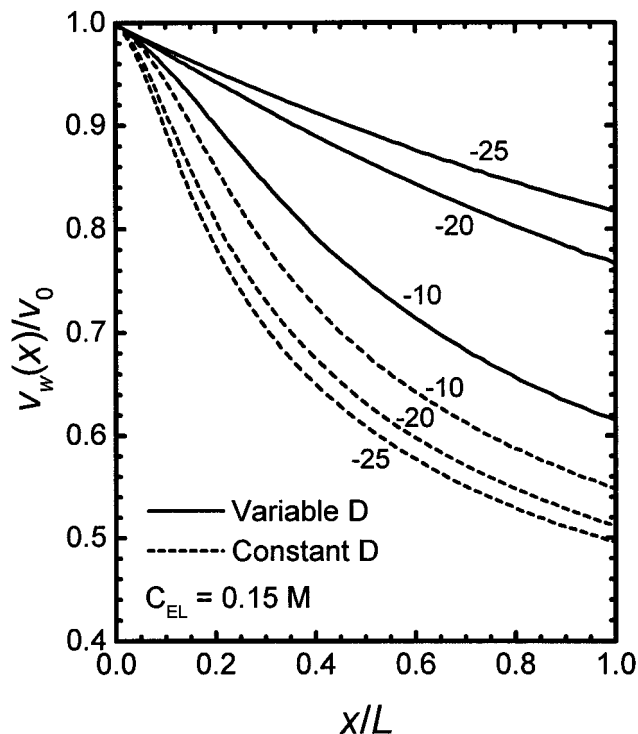


FIG. 12. Comparison of the predictions of the local variation of scaled permeate flux in a cross-flow filtration unit obtained using concentration dependent diffusivity (solid lines) and constant diffusivity (dashed lines) in the convective diffusion equation for different particle charges. The membrane permeability was 6.0×10^{-11} mPa $^{-1}$ s $^{-1}$. The channel length was 0.5 m. The operating conditions were fixed at $\Delta P = 250$ kPa, $\dot{\gamma} = 200$ s $^{-1}$, $T = 298$ K, $r_p = 3$ nm, and $\phi_b = 0.001$.

equation can, in fact, result in qualitatively incorrect predictions of the dependence of permeate flux on solution properties like electrolyte concentration and particle charge. This limitation of the constant diffusivity model is illustrated in Figs. 12 and 13, which depict the predictions of permeate flux at different particle charge and background electrolyte concentration, respectively. In these figures, the dashed lines were obtained using appropriate concentration dependencies of the osmotic pressure corresponding to each electrolyte concentration or particle charge, but using a constant Stokes–Einstein diffusion coefficient. The solid lines were obtained by additionally considering the concentration dependence of diffusivity. It is evident from the figures that the constant diffusivity model yields a qualitatively wrong prediction of the permeate flux decline behavior, indicating that the permeate flux decreases with increasing repulsion between the solute particles. The variable diffusivity model, however, predicts an entirely opposite behavior, indicating that an enhancement in interparticle repulsion (engendered by increasing the particle charge number or lowering the electrolyte concentration) results in a higher permeate flux.

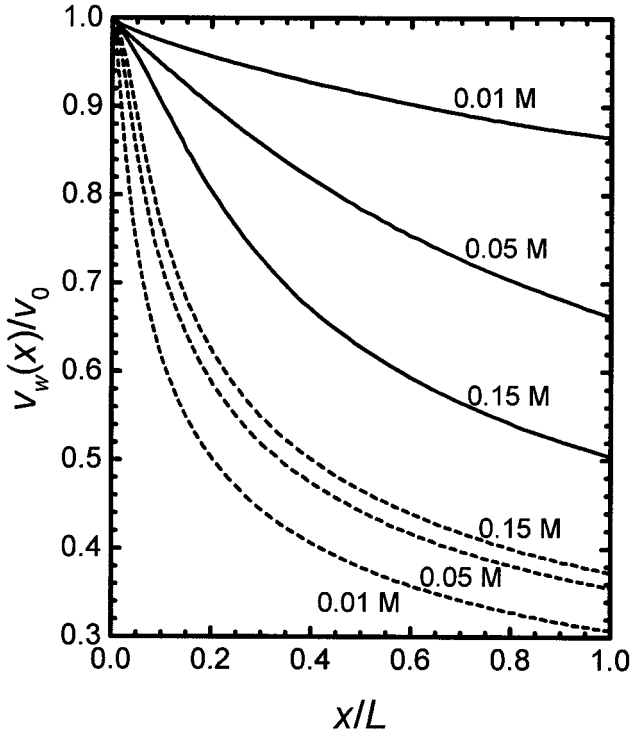


FIG. 13. Variation of the scaled permeate flux with scaled axial position in the cross-flow filtration cell predicted using variable and constant diffusion coefficient in the convective-diffusion equation. The predictions were obtained for a fixed charge number $z_p = -20$ on the particles but for different electrolyte concentrations as indicated in the figure. Operating conditions are same as in Fig. 12.

5.3. Influence of Particle Size on the Permeate Flux Decline

So far, we have considered a single particle size ($r_p = 3$ nm) in all the calculations. In this section, the influence of particle size on the extent of concentration polarization and the ensuing permeate flux decline behavior is illustrated. When the particle size increases, both the Stokes–Einstein diffusivity and the bulk osmotic pressure decrease. A decrease in the diffusion coefficient should result in lower solute back transport, thereby leading to severe concentration polarization. The osmotic pressure of a solution, on the other hand, increases nonlinearly with solute concentration and diverges at very high concentrations, implying that the permeate flux should be drastically lowered at high membrane surface concentrations of the solute particles. The influence of particle size on the permeate flux decline is manifested as a coupled effect of these two properties. The combined influence of osmotic pressure and diffusion coefficient on the permeate flux decline becomes more complex when the diffusion coefficient varies with solute concentration.

The effect of particle size becomes even more complicated in presence of long-range colloidal interactions, in which case the range of the interaction relative to the particle size also plays a significant role in governing the extent of concentration polarization and permeate flux decline. When the particle size

is much larger than the range of the interaction energy, the solution should behave somewhat like a hard-sphere system. For smaller particles, however, the range of the interaction energy will significantly influence the extent of osmotic pressure buildup and the variation of diffusivity. For instance, presence of long-range repulsion between the particles will result in a rapid increase of diffusion coefficient and osmotic pressure with particle concentration compared to hard-spherical particles.

Typical predictions of the channel-averaged permeate flux in a cross-flow filtration unit are depicted in Fig. 14 for different particle size and electrolyte concentrations. The channel-averaged permeate flux was obtained from the local permeate flux using

$$\langle v \rangle = \frac{1}{L} \int_0^L v_w(x) dx, \quad [5.1]$$

where L represents the channel length. The solid lines were obtained considering the concentration dependence of the dif-

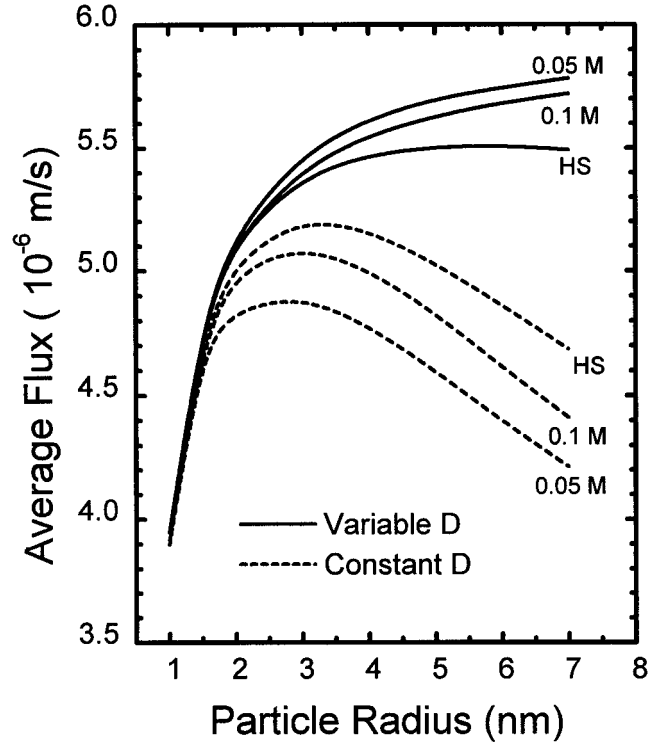


FIG. 14. Variation of the average permeate flux with particle radius for hard spherical (HS) and charged particles (at two different electrolyte concentrations) obtained on the basis of variable diffusivity (solid lines) and constant diffusivity (dashed lines) concentration polarization models. The operating conditions are: $\Delta P = 100$ kPa, $\dot{\gamma} = 600$ s $^{-1}$, $T = 298$ K, and $\phi_b = 0.01$. The membrane permeability and the channel length were fixed at 6.0×10^{-11} mPa $^{-1}$ s $^{-1}$ and 0.5 m, respectively, in all the calculations. The particle charge density was fixed at -20 mC/m 2 in all the calculations.

fusion coefficient in the convective-diffusion equation, while the dashed lines were obtained for constant (Stokes–Einstein) diffusivity. The concentration dependence of the osmotic pressure and the diffusion coefficient were obtained for various particle radii (ranging from 1 to 7 nm) and a fixed particle surface charge density ($q = z_p e / 4\pi r_p^2$) of -20 mC/m^2 .

Figure 14 indicates that the average permeate flux obtained using a constant diffusivity in the convective diffusion equation exhibits a maximum for particle size between 2 and 4 nm. The average permeate flux also depends on the range of the interaction energy, as shown by the lower permeate fluxes at lower electrolyte concentrations. The decrease in permeate flux with increasing particle size is a standard feature of the constant diffusivity model and is also observed using the traditional film theory (13). Experimentally observed permeate flux for repulsive colloidal systems, however, generally increases with particle size (11, 13). The predictions based on variable diffusivity (solid lines) are in qualitative agreement with these experimental trends. In this case, the permeate flux increases with increasing particle size and decreasing ionic strengths. These observations once again indicate that the convective-diffusion equation with a constant diffusivity may yield qualitatively and quantitatively incorrect predictions of the permeate flux decline behavior.

The size range of the particles and the operating conditions used to obtain the average permeate flux in Fig. 14 were selected such that a cake does not form on the membrane, and the flux decline is solely osmotic pressure governed. In our calculations, it was assumed that as long as the particle volume fraction at the membrane surface was less than 0.55, the filtration process could be considered as osmotic pressure governed. This was the case in all the flux predictions shown, with the particle volume fraction being much less than 0.55 at lower electrolyte concentrations. Based on the predictions of Fig. 14, it is evident that the membrane surface concentrations under a given set of conditions were much lower for the variable diffusivity model than those for the constant diffusivity model. This also implies that the enhancement of diffusivity can increase the domain of osmotic pressure governed membrane filtration. In other words, for a given solute particle dispersion, a cake (gel) layer would form at higher pressures when the diffusion coefficient increases with particle concentration.

5.4. Flux-Pressure Relationship for Concentration Dependent Diffusivity

Figure 15 depicts the variation of the channel-averaged permeate flux with operating pressure obtained using constant and variable diffusivity in the convective diffusion equation for different particle sizes. In these calculations, the operating pressure range was selected to ensure that a cake layer does not form on the membrane surface. Under these conditions, the constant diffusivity model predicts a nearly pressure-indepen-

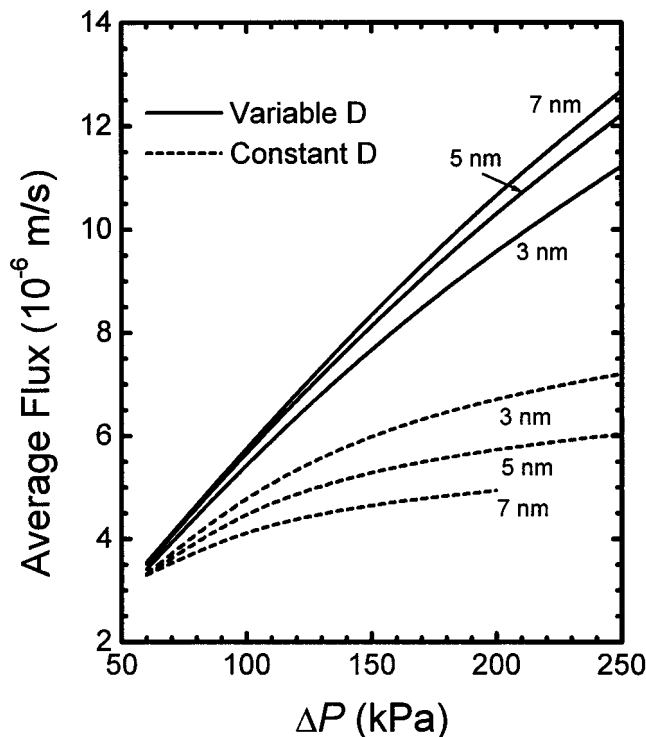


FIG. 15. Variation of the average permeate flux with operating pressure obtained for different particle size. The particle charge density and background electrolyte concentration were fixed at -20 mC/m^2 and 0.05 M , respectively. Other operating parameters are same as in Fig. 14.

dent flux over the pressure range considered. Furthermore, the permeate flux becomes lower as the particle size is increased. The predictions based on concentration dependent diffusivity are, however, pressure dependent, and increase marginally as the particle size is increased. The figure also shows that for a particle radius of 7 nm, the permeate flux decline behavior using constant diffusivity possibly becomes cake layer controlled beyond $\Delta P = 200 \text{ kPa}$, since above this pressure the particle volume fraction at the membrane surface attains the maximum value of 0.55. The corresponding dashed line is truncated at this pressure. The permeate flux obtained using variable diffusivity, however, remains osmotic pressure governed up to considerably higher pressures as the membrane surface volume fraction remains substantially lower than 0.55 in this case.

6. SUMMARY AND CONCLUDING REMARKS

A comprehensive theoretical approach for predicting the influence of physicochemical interactions between solute particles on the permeate flux decline during cross-flow membrane filtration of small colloidal or macromolecular solute particles has been presented. The approach draws upon the integral equation theory of statistical mechanics to predict the solution structure (represented as the pair correlation function) using a

pairwise summation of the binary interactions between the solute particles. The resulting pair correlation function is used in the virial equation of state and a theory of batch sedimentation to predict the osmotic compressibility and the sedimentation coefficient, respectively. The osmotic pressure and sedimentation coefficient are then used to obtain the concentration dependence of the diffusion coefficient. Incorporation of the concentration dependence of osmotic pressure and diffusion coefficient in the framework of the convective-diffusion equation coupled with the osmotic pressure model for permeate flow leads to the prediction of permeate flux decline due to concentration polarization.

It is important to consider the variations of diffusivity in the convective diffusion equation in order to predict the permeate flux decline behavior accurately. The variable diffusivity model is particularly necessary to elucidate the influence of the physicochemical interactions between the solute particles in a concentrated dispersion on permeate flux decline. The predictions indicate an enhancement of permeate flux in presence of interparticle repulsion. This is predominantly due to the enhanced diffusive back-transport of solutes in the polarized layer, which lowers the extent of concentration polarization. Consequently, although the osmotic pressure buildup increases in presence of large interparticle repulsion, the permeate flux may actually increase due to a less significant buildup of membrane surface concentration. The counteracting effects of osmotic pressure and diffusion coefficient, however, limit the extent of permeate flux variation attainable by changing the physicochemical properties of the solution. This is evident at low electrolyte concentrations where, although both diffusivity and osmotic compressibility are enhanced by factors of 10–100 at high volume fractions, the corresponding enhancement in permeate flux is relatively modest.

The approach presented here provides a significantly broader perspective of the influence of interparticle interactions on the solution properties in a polarized layer and the ensuing permeate flux decline behavior. The unification of the continuum approach for modeling concentration polarization and the statistical mechanical approach for predicting the thermodynamic and transport properties provides a direct quantitative link between the interparticle interactions and the permeate flux decline. As a consequence, the theoretical model presented here shifts the experimental focus in membrane filtration studies from measurement of osmotic pressure and diffusion coefficient to more fundamental measurements of the parameters governing the interparticle interactions between the solute particles.

APPENDIX A: NUMERICAL SOLUTION OF THE ORNSTEIN-ZERNIKE INTEGRAL EQUATION

For radially symmetric interaction potentials, the correlation functions in the OZ integral equation are radially symmetric. Consequently, the three-dimensional correlation functions can

be expressed as one-dimensional functions of radial position alone.

The Fourier transform of a radially symmetric function $\gamma(r)$ can be written as a one-dimensional sine transform (37)

$$\tilde{\gamma}(k) = 4\pi \int_0^\infty r^2 \gamma(r) \frac{\sin(kr)}{kr} dr, \quad [\text{A.1}]$$

the inverse transform being

$$\gamma(r) = \frac{1}{2\pi^2} \int_0^\infty k^2 \tilde{\gamma}(k) \frac{\sin(kr)}{kr} dk, \quad [\text{A.2}]$$

where the presence of a tilde denotes the Fourier transformed function. From Eqs. [A.1] and [A.2], it is clear that a function F , defined as

$$F(r) = r\gamma(r) \quad [\text{A.3}]$$

can be Fourier transformed using any standard numerical algorithm for treatment of one-dimensional sine transforms. Following is a brief description of the numerical technique employed in this study to solve the OZ equation with the PY and HNC closures.

The real space $r(0 \leq r \leq \gamma_{\max})$, where γ_{\max} is a suitably chosen large value) is discretized into N intervals, the location of each point being

$$r_i = i\Delta r, \quad i = 1, 2, \dots, N, \quad [\text{A.4}]$$

where Δr is the step size. The step size in the Fourier transformed domain is related to Δr as

$$\Delta k = \frac{\pi}{N\Delta r}, \quad [\text{A.5}]$$

with the discrete Fourier space variable k given by

$$k_j = j\Delta k, \quad j = 1, 2, \dots, N. \quad [\text{A.6}]$$

The discrete Fourier sine transform pair corresponding to Eqs. [A.1] and [A.2] can now be written as

$$\begin{aligned} \tilde{F}_j &= 4\pi\Delta r \sum_{i=1}^{N-1} F_i \sin\left(\frac{\pi ij}{N}\right), \quad j = 1, 2, \dots, N-1 \\ F_i &= \frac{\Delta k}{2\pi^2} \sum_{j=1}^{N-1} \tilde{F}_j \sin\left(\frac{\pi ij}{N}\right), \quad i = 1, 2, \dots, N-1. \end{aligned} \quad [\text{A.7}]$$

The above Fourier transformations can be performed using discrete sine transformation techniques that utilize fast Fourier transforms (47).

Writing the various correlation functions as $C_i = r_i c_i$, $H_i = r_i h_i$, and $\Gamma_i = r_i \gamma_i$, where $\gamma_i = h_i - c_i$, the PY and HNC closures are expressed as

$$C_i = r_i \left[\exp\left(\frac{\Gamma_i}{r_i}\right) - \frac{\Gamma_i}{r_i} - 1 \right] \quad [\text{A.8}]$$

and

$$C_i = r_i \left[\exp\left(-\beta E(r) + \frac{\Gamma_i}{r_i}\right) - \frac{\Gamma_i}{r_i} - 1 \right], \quad [\text{A.9}]$$

respectively. Furthermore, Fourier transformation of the OZ Eq. [2.6] yields

$$\tilde{\Gamma}_j = \frac{n\tilde{C}_j^2}{k_j - n\tilde{C}_j}. \quad [\text{A.10}]$$

Equation [A.10], along with an appropriate closure, Eq. [A.8] or Eq. [A.9], can be solved by a Picard iteration technique. The solution procedure starts with an initial guess of the function Γ_i . Substitution of this initial guess in the closure equation provides an estimate of C_i , which is Fourier transformed to obtain \tilde{C}_j . Substitution of \tilde{C}_j in Eq. [A.10] provides $\tilde{\Gamma}_j$, which is back transformed to obtain an updated value of $\Gamma_i^{(2)}$. This new estimate of Γ_i is compared with the old estimate. If the difference between the two values is less than a predefined convergence criterion at every point in the r space, the solution is assumed to have converged. Otherwise, a new weighted guess for the value of Γ_i is evaluated using

$$\Gamma_i^{(\text{new})} = \omega \Gamma_i^{(2)} + (1 - \omega) \Gamma_i, \quad [\text{A.11}]$$

where ω is a weighting parameter ($0 < \omega < 1$). The use of an appropriate weighting parameter is a key to the success of the above Picard iteration scheme. When the value of ω is set to 1, the solution often becomes oscillatory and fails to converge. Consequently a smaller value of the parameter is required, which ensures a stable, albeit slower, convergence. Once the solution has converged, the pair correlation function can be determined using

$$g_i = 1 + h_i. \quad [\text{A.12}]$$

The above numerical scheme is quite efficient in a fast processor, and for the systems studied in this work, its results are identical to those obtained from more sophisticated algorithms (48). It is important to note that the simple algorithm described here is suitable only when the interaction energy is

relatively short ranged compared to the particle dimensions. Application of the algorithm for long ranged interactions (for instance, in electrolyte systems interacting through unscreened Coulomb potential) requires modifications to correct the long-range inaccuracies arising from the discrete Fourier transform techniques (48). Details of such corrections are available elsewhere (35, 48, 49).

APPENDIX B: NUMERICAL SOLUTION OF THE VARIABLE-DIFFUSIVITY CONVECTIVE-DIFFUSION EQUATION

The governing equations for concentration polarization were solved using the method of lines (50). The convective-diffusion Eq. [2.1] was written in a nondimensional form as

$$\frac{\partial \theta}{\partial X} = \frac{\zeta}{Y} \left[\frac{\partial}{\partial Y} \left(F(\theta) \frac{\partial \theta}{\partial Y} \right) - \hat{\text{Pe}} \frac{\partial \theta}{\partial Y} \right], \quad [\text{B.1}]$$

using the scaled variables

$$\theta = \frac{n}{n_b}, \quad X = \frac{x}{L}, \quad Y = \frac{y}{\delta}, \quad \hat{\text{Pe}} = \frac{v\delta}{D_\infty}, \quad [\text{B.2}]$$

where L and δ represent the channel length and the thickness of polarized boundary layer, respectively. The parameter ζ is given as

$$\zeta = \frac{LD_\infty}{\dot{\gamma}\delta^3}, \quad [\text{B.3}]$$

where $\dot{\gamma}$ is the shear rate used to define the axial (crossflow) velocity profile as

$$u = \dot{\gamma}y. \quad [\text{B.4}]$$

The function $F(\theta)$ denotes the concentration dependent part of the diffusion coefficient and is expressed as

$$F(\theta) = \frac{D(\theta)}{D_\infty}. \quad [\text{B.5}]$$

Equation [B.1] was discretized in the Y domain by employing a finite difference scheme, thereby yielding a set of coupled nonlinear ordinary differential equations (ODEs) in the X domain. The general form of the ordinary differential equations is

$$\frac{d\theta_k}{dX} = \frac{\zeta}{Y_k} \left\{ \frac{2}{(h_{k+1} + h_k)} \left[F\left(\frac{\theta_{k+1} + \theta_k}{2}\right) \frac{(\theta_{k+1} - \theta_k)}{h_{k+1}} - F\left(\frac{\theta_k + \theta_{k-1}}{2}\right) \frac{(\theta_k - \theta_{k-1})}{h_k} \right] - \hat{\text{Pe}} \frac{(\theta_{k+1} - \theta_{k-1})}{(h_{k+1} + h_k)} \right\}. \quad [\text{B.6}]$$

Here, θ_k represents the scaled concentration at the finite difference point k , where the local Y is represented by Y_k . The above finite difference formula employs a nonuniform grid. It should be noted that the function $F(\theta)$ was quasi-linearized over each finite difference interval h_k ($= Y_k - Y_{k-1}$) (47). The set of coupled ordinary differential equations represented by Eq. [B.6], along with the appropriate boundary conditions obtained using the discretized forms of Eqs. [2.2] and [2.3], were solved using a backward difference predictor–corrector method which is suitable for stiff ODEs (51).

The boundary layer thickness δ must be known a priori to obtain a solution of the above system of equations. A conservative estimate of the latter may be about 10–20% of the half-channel height (52, 53). Using a larger value of δ does not alter the concentration profile, although lower values of this parameter may result in erroneous predictions of the concentration profile and the permeate flux depending on other operating conditions. In this study, δ was ascertained by assuming that the concentration profile becomes flat (that is, the slope of the concentration profile $d\theta/dY \rightarrow 0$) at $y = \delta$. In the computer implementation, the value of δ was increased until the slope at $y = \delta$ became smaller than a preset limit ϵ .

APPENDIX C: NOMENCLATURE

A	Hamaker constant (J)
A_{ij}, B_{ij}	hydrodynamic interaction parameters used in Eq. [2.10]
a_i	coefficients used in Eq. [4.4]
C_{EL}	electrolyte concentration (M)
$c(r)$	direct correlation function
D	gradient diffusion coefficient (m^2/s)
D_∞	Stokes–Einstein diffusivity (m^2/s)
E	pair interaction potential (J)
e	electronic charge (1.6×10^{-19} C)
$F(\theta)$	concentration dependent part of diffusivity given by Eq. [B.5]
$g(r)$	pair correlation function (radial distribution function)
$g_{ss}(r)$	Boltzmann distribution function
$h(r)$	total correlation function
h_k	finite difference step size at k th node
K	sedimentation coefficient
k	Boltzmann constant (1.38×10^{-23} JK $^{-1}$)
L	length of crossflow filtration channel (m)
N_A	Avogadro number (6.023×10^{23})
n	particle concentration (m^{-3})
Pe	local Peclet Number
$\hat{P}e$	Peclet Number in membrane filtration channel, Eq. [B.2]
q	charge density (C/m^2)
R	scaled radial distance (r/σ)
R_m	membrane hydraulic resistance (m^{-1})
r	radial position
r_p	particle radius

s	scaled distance (r/r_p)
T	temperature (K)
u	cross-flow velocity (m/s)
$v(x)$	transverse velocity of the permeate (m/s)
v_0	pure solvent flux (m/s)
v_w	permeate flux (m/s)
$\langle \hat{v} \rangle$	average permeate flux (m/s)
X	dimensionless axial distance, Eq. [B.2]
x	axial direction in a crossflow filtration unit
Y	dimensionless transverse distance, Eq. [B.2]
y	transverse direction in a crossflow filtration unit
Z	osmotic compressibility
z	valence of background electrolyte
z_p	particle charge number

Greek Symbols

α	exponent in Eq. [2.8]
β	$1/kT$ (J^{-1})
$\dot{\gamma}$	shear rate (s^{-1})
$\gamma(r)$	$h(r) - c(r)$
$\tilde{\gamma}$	Fourier transformed $\gamma(r)$
δ	polarized layer thickness
ϵ_0	dielectric permittivity of vacuum (8.854×10^{-12} C 2 N $^{-1}$ m $^{-2}$)
ϵ_r	relative dielectric permeability of solvent
ϕ	particle volume fraction
κ^{-1}	Debye screening length (m)
μ	solvent viscosity (N s m $^{-2}$)
Π	osmotic pressure
θ	dimensionless concentration defined in Eq. [B.2]
σ	particle diameter
σ_o	osmotic reflection coefficient
ω	weighting factor in Picard iteration technique
ζ	dimensionless parameter in Eq. [B.3]

Subscripts

b	bulk solution
EL	electrolyte
m	membrane surface
p	permeate

REFERENCES

1. Bowen, W. R., and Jenner, F., *Adv. Colloid Interface Sci.* **56**, 141 (1995).
2. Van den Berg, G. B., and Smolders, C. A., *Desalination* **77**, 101 (1990).
3. Vilker, V. L., Colton, C. K., and Smith, K. A., *AIChE J.* **27**, 637 (1981).
4. Bhattacharjee, S., Sharma, A., and Bhattacharya, P. K., *J. Membr. Sci.* **111**, 243 (1996).
5. Elimelech, M., and Bhattacharjee, S., *J. Membr. Sci.* **145**, 223 (1998).
6. Wijmans, J. G., Nakao, S., van den Berg, J. W. A., Troelstra, F. R., and Smolders, C. A., *J. Membr. Sci.* **22**, 117 (1985).
7. Song, L., and Elimelech, M., *J. Chem. Soc. Faraday Trans.* **91**, 3389 (1995).

8. Bhattacharjee, S., Sharma, A., and Bhattacharya, P. K., *Langmuir* **10**, 4710 (1994).
9. Wijmans, J. G., Nakao, S., and Smolders, C. A., *J. Membr. Sci.* **20**, 115 (1984).
10. McDonogh, R. M., Fell, C. J. D., and Fane, A. G., *J. Membr. Sci.* **21**, 285 (1984).
11. McDonogh, R. M., Fell, C. J. D., and Fane, A. G., *J. Membr. Sci.* **43**, 69 (1989).
12. McDonogh, R. M., Welsch, K., Fell, C. J. D., and Fane, A. G., *J. Membr. Sci.* **72**, 197 (1992).
13. Welsch, K., McDonogh, R. M., Fane, A. G., and Fell, C. J. D., *J. Membr. Sci.* **99**, 229 (1995).
14. Bowen, W. R., and Jenner, F., *Chem. Eng. Sci.* **50**, 1707 (1995).
15. Bowen, W. R., Mongruel, A., and Williams, P. M., *Chem. Eng. Sci.* **51**, 4321 (1996).
16. Petsev, D. N., Starov, V. M., and Ivanov, I. B., *Colloids Surf. A* **81**, 65 (1993).
17. Jonsson, A-S., Jonsson, B., *J. Colloid Interface Sci.* **180**, 504 (1996).
18. Holt, W. J. C., Carnie, S. L., and Chan, D. Y. C., *J. Colloid Interface Sci.* **173**, 304 (1995).
19. Happel, J., *AIChE J.* **4**, 197 (1958).
20. Happel, J., and Brenner, H., "Low Reynolds Number Hydrodynamics." Kluwer, Dordrecht, 1991.
21. Batchelor, G. K., *J. Fluid Mech.* **52**, 245 (1972).
22. Denkov, N. D., and Petsev, D. N., *Physica A* **183**, 462 (1992).
23. Genz, U., and Klein, R., *Physica A* **171**, 26 (1991).
24. Russel, W. B., and Glendinning, A. B., *J. Chem. Phys.* **74**, 948 (1981).
25. Russel, W. B., Saville, D. A., and Schowalter, W. R., "Colloidal Dispersions." Cambridge Univ. Press, Cambridge, 1989.
26. Dhont, J. K. G., "An Introduction to Dynamics of Colloids." Elsevier, Amsterdam, 1996.
27. Xu, W., Nikolov, A., and Wasan, D. T., *J. Colloid Interface Sci.* **197**, 160 (1998).
28. Batchelor, G. K., *J. Fluid Mech.* **74**, 1 (1976).
29. Hansen, J. P., and McDonald, I. R., "Theory of Simple Liquids." Academic Press, London, 1976.
30. Ornstein, L. S., and Zernike, F., *Proc. Akad. Sci. (Amsterdam)* **17**, 793 (1914).
31. Percus, J. K., and Yevick, G. J., *Phys. Rev.* **110**, 1 (1958).
32. Van Leeuwen, J. M. J., Groeneveld, J., and De Boer, J., *Physica* **25**, 792 (1959).
33. Derjaguin, B. V., and Landau, L., *ACTA Physicochim.* **14**, 633 (1941).
34. Verwey, E. J. W., and Overbeek, J. Th. G., "Theory of Stability of Lyophobic Colloids." Elsevier, Amsterdam, 1948.
35. Vlachy, V., and Prausnitz, J. M., *J. Phys. Chem.* **96**, 6465 (1992).
36. Vlachy, V., Pohar, C., and Haymet, A. D. J., *J. Chem. Phys.* **88**, 2066 (1988).
37. Allen, M. P., and Tildesley, D. J., "Computer Simulation of Liquids." Oxford Univ. Press, New York, 1987.
38. Carnahan, N. F., and Starling, C. S., *J. Chem. Phys.* **51**, 635 (1969).
39. Russel, W. B., "The Dynamics of Colloidal Systems." The Univ. of Wisconsin Press, Madison, WI, 1987.
40. Buscall, R., Goodwin, J. W., Ottewill, R. H., and Tadros, T. F., *J. Colloid Interface Sci.* **85**, 78 (1982).
41. de Kruijff, C. G., Jansen, J. W., and Vrij, A., in "Physics of Complex and Supramolecular Fluids" (S. A. Safran and N. A. Clark, Eds.). Wiley Interscience, New York, 1987.
42. Petsev, D. N., and Denkov, N. D., *J. Colloid Interface Sci.* **149**, 329 (1992).
43. Anderson, J. L., Rauh, F., and Morales, A., *J. Phys. Chem.* **82**, 608 (1978).
44. Phillies, G. D. J., Benedek, G. B., and Mazer, N. A., *J. Chem. Phys.* **65**, 1883 (1976).
45. Hunter, R. J., "Foundations of Colloid Science," Vol. 1. Oxford Univ. Press, New York, 1986.
46. Vilker, V. L., Colton, C. K., and Smith, K. A., *J. Colloid Interface Sci.* **79**, 548 (1981).
47. Press, W. H., Teukolsky, S. A., Vetterling, W. T., and Flannery, B. P., "Numerical Recipes in Fortran: The Art of Scientific Computing," 2nd ed. Cambridge Univ. Press, New York, 1992.
48. Labik, S., Malijevsky, A., and Vonka, P., *Mol. Phys.* **56**, 709 (1985).
49. Abernethy, G. M., and Gillan, M. J., *Mol. Phys.* **39**, 839 (1980).
50. Zwillinger, D., "Handbook of Differential Equations," 3rd ed. Academic Press, San Diego, 1998.
51. Petzold, L. R., "A Description of DASSL: A Differential/Algebraic System Solver," SAND82-8637. Sandia National Laboratories, 1982.
52. Bouchard, C. R., Carreau, P. J., Matsuura, T., and Sourirajan, S., *J. Membrane Sci.* **97**, 215 (1994).
53. De, S., Bhattacharjee, S., Sharma, A., and Bhattacharya, P. K., *J. Membrane Sci.* **130**, 99 (1997).